

See discussions, stats, and author profiles for this publication at: <https://www.researchgate.net/publication/266318928>

# In Situ Synthesis of Three-Dimensional Self-Assembled Metal Oxide– Reduced Graphene Oxide Architecture

ARTICLE in CHEMISTRY OF MATERIALS · AUGUST 2014

Impact Factor: 8.35 · DOI: 10.1021/cm5020898

---

CITATIONS

13

---

READS

62

## 8 AUTHORS, INCLUDING:



[Hyun-Kyung Kim](#)

University of Cambridge

28 PUBLICATIONS 180 CITATIONS

[SEE PROFILE](#)



[Sang Hoon Park](#)

Yonsei University

19 PUBLICATIONS 140 CITATIONS

[SEE PROFILE](#)



[Chang Wook Lee](#)

Argonne National Laboratory

13 PUBLICATIONS 246 CITATIONS

[SEE PROFILE](#)



[Kibuem Kim](#)

Sejong University

267 PUBLICATIONS 3,470 CITATIONS

[SEE PROFILE](#)

# In Situ Synthesis of Three-Dimensional Self-Assembled Metal Oxide–Reduced Graphene Oxide Architecture

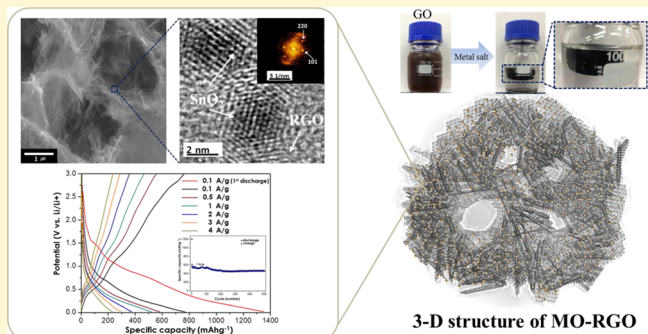
Hyun-Kyung Kim,<sup>†</sup> Sang-Hoon Park,<sup>†</sup> Seung-Beom Yoon,<sup>†</sup> Chang-Wook Lee,<sup>†</sup> Jun Hui Jeong,<sup>†</sup> Kwang Chul Roh,<sup>\*,‡</sup> and Kwang-Bum Kim<sup>\*,†</sup>

<sup>†</sup>Department of Materials Science and Engineering, Yonsei University, 134 Shinchon-dong, Seodaemun-gu, Seoul, Republic of Korea

<sup>‡</sup>Energy Efficient Materials Team, Energy & Environmental Division, Korea Institute of Ceramic Engineering & Technology, 233-5 Gasan-dong, Guemcheon-gu, Seoul, Republic of Korea

## Supporting Information

**ABSTRACT:** The fabrication of self-assembled, three-dimensional (3-D) graphene structures is recognized as a powerful technique for integrating various nanostructured building blocks into macroscopic materials. In this way, nanoscale properties can be harnessed to provide innovative functionalities of macroscopic devices with hierarchical microstructures. To this end, we report on the fabrication of a three-dimensional (3-D) metal oxide (MO)–reduced graphene oxide (RGO) architecture by controlling the reduction conditions of graphene oxide. In this structure, SnO<sub>2</sub> nanoparticles with dimensions of 2–3 nm are uniformly anchored and supported on a 3-D RGO structure. The resulting composite exhibits excellent rate capability as a binder-free electrode and shows great potential for use in Li-ion batteries. Furthermore, the proposed reduction synthesis can also be applied to the study of the synergistic properties of other 3-D MO–RGO architectures.



## INTRODUCTION

The structure of graphene, a single layer of carbon atoms patterned in a hexagonal lattice, results in an unusual combination of characteristics including outstanding electronic properties, high thermal conductivity, good optical properties, high mechanical strength, and a large surface area. As such, graphene has attracted considerable attention worldwide for potential applications in sensors, catalysis, energy-storage devices, and environmental fields. Although most of this previous research has focused on two-dimensional (2-D) specimens and devices,<sup>1–3</sup> these 2-D graphene sheets must be integrated into macroscopic 3-D structures to take full advantage of their properties and associated benefits.<sup>4,5</sup>

Of the available techniques for integrating nanostructured building blocks into macroscopic materials, the fabrication of self-assembled, 3-D graphene structures has been recognized as one of the most effective, as it is capable of harnessing nanoscale properties to provide novel functionalities of hierarchically structured macroscopic devices. Furthermore, superstructures assembled in this way exhibit unique collective physiochemical properties different from those of the individual components and bulk material, which help enrich the variety of graphene-based materials and broaden their capacity for practical application.<sup>6–8</sup> A number of different interactions such as dipole interactions, electrostatic attraction, or repulsion, hydrophilic/hydrophobic interactions, and hydrogen bonding have also been utilized in the self-assembly process itself.

Studies pertaining to composites of graphene and nanoparticles have flourished in recent years, as such materials combine the advantages of both graphene and nanoparticles and therefore have potential for application in catalysis, sensors, and energy fields.<sup>9–13</sup> More recently, the capture of preprepared metal oxide nanoparticles or metal salts in 3-D graphene networks has been reported as possible with the assistance of a suitable reducing agent (NaHSO<sub>3</sub>, Na<sub>2</sub>S, vitamin C, HI, and hydroquinone).<sup>14,15</sup>

In most previous studies, nanometer-sized 3-D structured metal oxide (MO)–graphene has been synthesized by physically mixing the MO with graphene oxide (GO), dispersing it in an aqueous solution, and then adding a reducing agent. In this process, MO particles are randomly captured and aggregated between the graphene sheets, which significantly inhibits their nanoscale effects.<sup>14,16</sup> Consequently, most such materials are instead prepared from 2-D graphene nanosheets onto which nanoparticles have been deposited or adsorbed, and there are still very few reports on different routes for directly preparing 3-D graphene–nanoparticle composites.<sup>17</sup>

With this in mind, we herein report on a self-assembled, 3-D RGO architecture that is prepared with electrochemically active

Received: June 8, 2014

Revised: July 28, 2014

Published: August 5, 2014



MO nanoparticles ( $\text{SnO}_2$ ) interfacially anchored between highly conductive RGO structures. This was achieved with a simple one-pot synthesis in which a metal salt ( $\text{SnCl}_2$ ) was used not only as a reducing agent to transform GO into highly conductive 3-D RGO but also as a precursor to form a 3-D metal oxide ( $\text{SnO}_2$ ) structure under carefully controlled reduction conditions. The 3D  $\text{SnO}_2$ -RGO composite synthesized in this manner is electrochemically assessed for use as a binder-free anode in high-rate Li-ion batteries. Further, the adaptability of this method is demonstrated by using other metal salts such as  $\text{VCl}_3$  and  $\text{RuCl}_3$  to synthesize  $\text{V}_2\text{O}_5$  and  $\text{RuO}_2$ .

## EXPERIMENTAL SECTION

**Preparation of 3-D MO-RGO Architecture.** For the preparation of 3-D  $\text{SnO}_2$ -RGO nanocomposites with varying amounts of  $\text{SnO}_2$ , 120 mg of GO powder (synthesized by Hummer's method) was first ultrasonicated in 60 mL of deionized water. The resulting GO suspension was then equally separated into seven identical bottles, and the contents of each was then mixed with a different weight of  $\text{SnCl}_2$  powder (98%, Aldrich) to control the  $\text{SnO}_2$  loading ( $\text{Sn}/\text{GO} = 0:1$ , 1:10, 1:5, 1:2, 1:1, 2:1, and 5:1). To prepare 3-D  $\text{V}_2\text{O}_5$  or  $\text{RuO}_2$ -RGO nanocomposites, the contents of each bottle were mixed with  $\text{VCl}_3$  and  $\text{RuCl}_3$  powders (85%, Aldrich) to a V/GO or Ru/GO ratio of 2:1 by weight. These mixtures were all stirred for 5 min at room temperature (25 °C) and then for 8 h in an oven at 85 °C. The products were then washed several times with distilled water and ethanol to remove any residual chloride ions and other impurities. Finally, the powders were dried in an oven at 70 °C for 4 h and then freeze-dried for 24 h.

**Characterization Methods.** The structure and morphology of the resulting samples were characterized using scanning electron microscopy (SEM; JSM-7001F, JEOL Ltd.), transmission electron microscopy (TEM; 200 kV; CM200, Philips), X-ray diffraction (XRD; Cu  $\text{K}\alpha$ , 40 kV, 20 mA; Rigaku), and Raman spectroscopy (LabRam, Jobin Yvon-Spex). In addition, the surfaces of all the samples were analyzed using Fourier transform infrared spectroscopy (FTIR; Vertex 70, Bruker) and X-ray photoelectron spectroscopy (XPS; 15 kV, 150 W; ESCALAB 250, Thermo Electron Corporation). Thermal data for the samples were collected using a thermogravimetric analyzer (STA 409 PC, Netzsch) operating in air from room temperature to 800 °C with a heating and cooling rate of 10 °C min<sup>-1</sup>. The room-temperature (25 °C) electrochemical properties of the samples were investigated using a CR2032 coin cell with metallic lithium as the cathode and a 1-mg binder-free electrode as the working electrode. The electrolyte was a 1 M solution of  $\text{LiPF}_6$  dissolved in equal weights of ethylene carbonate and dimethyl carbonate. The charge-discharge tests and cyclic voltammetry were performed using a potentiostat/galvanostat (VMP3, Princeton Applied Research). The  $\text{N}_2$  adsorption-desorption isotherms of the samples were measured at 77 K using a Micromeritics ASAP 2010 instrument.

## RESULTS AND DISCUSSION

Figure 1a,b shows the 3-D  $\text{SnO}_2$ -RGO composites synthesized by mixing various weights of tin salt and GO at room temperature (25 °C) or 85 °C, along with a schematic illustrating the protocol used for their synthesis. These results suggest that a 3-D  $\text{SnO}_2$ -RGO nanocomposite structure does not form at room temperature, regardless of the amount of  $\text{SnCl}_2$  used, and that only small building blocks were present between the RGO sheets (Figure S1 in the Supporting Information). However, at 85 °C, a black porous 3-D hydrogel is obtained when the amount of  $\text{SnCl}_2$  added exceeds a certain threshold. In this hydrogel, the  $\text{SnO}_2$  nanoparticles are anchored in the RGO networks, and the combined hydrophobic and  $\pi-\pi$  stacking interactions drive the development of a 3-D interconnected structure because the Sn ions dramatically

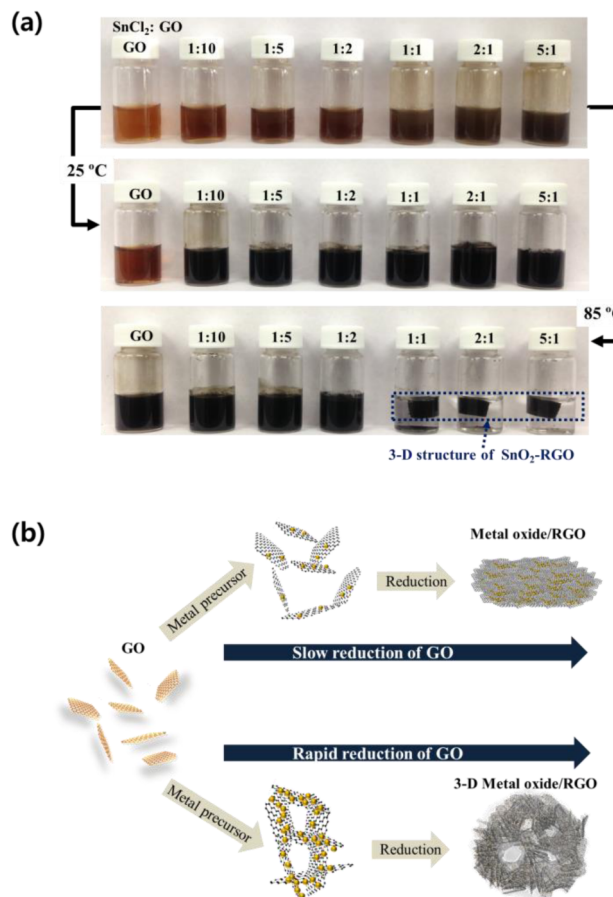


**Figure 1.** (a) Photographs of 3-D  $\text{SnO}_2$ -RGO nanostructures prepared with different weight ratios of  $\text{SnCl}_2$  and GO ( $\text{Sn}/\text{GO} = 1:10$ , 1:5, 1:2, 1:1, 2:1, and 5:1) at 25 and 85 °C. (b) Schematic illustrating the protocol used to synthesize 3-D architectures.

decrease the number of oxygenated groups on the GO sheets. This suggests that, in order to form a complete 3-D structure, the number of functional groups on the GO surface must be rapidly reduced below a certain threshold corresponding to the threshold number of Sn ions acting as reducing agents. Furthermore, when the hydrophilic graphene oxide surface instantly becomes hydrophobic, carbon atoms simultaneously compete to form  $\pi-\pi$  bonds, thereby enabling a rigid structure to form. In contrast, when the amount of reducing agent is low or the reduction proceeds slowly (as is the case at room temperature), the hydrophilic graphene oxide surface gradually becomes hydrophobic. In this case, the sequential formation of  $\pi-\pi$  bonds between carbon atoms prevents a 3-D structure from forming, and thus the overall arrangement consists of bonds between sheets or small structures. Consequently, even large quantities of GO and  $\text{SnCl}_2$  can be mixed to completely form a 3-D structured

In order to provide information on the reduction rate of GO, we investigated the effects of reaction temperatures at the fixed weight ratio of  $\text{SnCl}_2$  and GO of 2:1. Figure 2a,b shows XPS C 1s spectra of the 3-D  $\text{SnO}_2$ -RGO and the  $\text{SnO}_2$ /RGO composite (flakes) prepared at 85 and 25 °C, respectively, as a function of the reduction time allowed for the synthesis. At 85 °C, the intensity of the C-OH (286.7 eV) peak was observed to decrease even at the reaction time of 1 h. As the reaction time was increased up to 6 h, the intensities of the C-OH bond did not seem to decrease, indicating that the reduction of GO

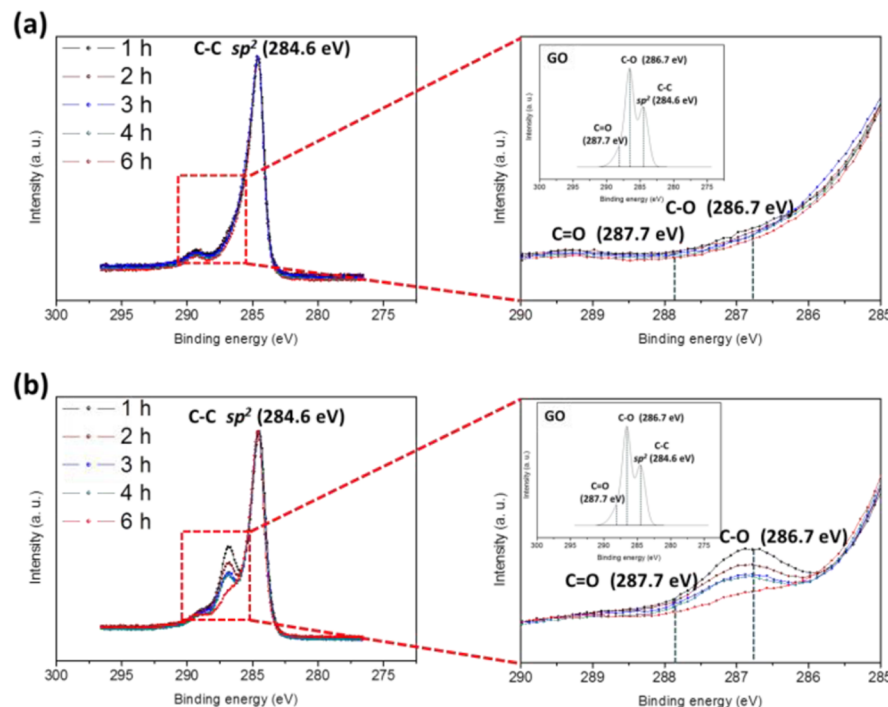


**Figure 2.** XPS C 1s spectra of (a) the 3-D  $\text{SnO}_2$ –RGO architecture and (b) the  $\text{SnO}_2$ /RGO composite (flakes) prepared using  $\text{SnCl}_2$  and GO (Sn/GO 2:1) at 85 and 25 °C, respectively. The inset shows the XPS C 1s spectra of the GO.

to RGO was completed within 1 h. On the other hand, at 25 °C, the gradual decrease in intensity of the C–OH peak was observed during 6 h, indicating that the reduction of GO to RGO proceeded slowly at 25 °C. From the above results, for the synthesis of 3-D  $\text{SnO}_2$ –RGO, GO is rapidly reduced in a short time to transform RGO by the tin salt.

Additionally, in order to compare with  $\text{SnO}_2$ /RGO composite and 3-D  $\text{SnO}_2$ –RGO architecture, we performed a gas adsorption measurement to investigate the specific surface area, pore size distribution and pore volume of the  $\text{SnO}_2$ /RGO composite and the 3-D  $\text{SnO}_2$ –RGO architecture. In the  $\text{N}_2$  adsorption–desorption isotherm of  $\text{SnO}_2$ /RGO composite shown in Figure S3a in the Supporting Information, there exists a knee for the first adsorption step around the relative vapor pressure of 0.1 and a small hysteresis loop at the relative vapor pressures of 0.4–0.8, which are the characteristic features of the type IV isotherm. It is expected that the pore structure should be originated from RGO flake.<sup>18</sup> The BET surface area was found to be  $280 \text{ m}^2 \text{ g}^{-1}$ , with a pore size of 3.21 nm and pore volume of  $0.14 \text{ cm}^3 \text{ g}^{-1}$ . Figure S3b in the Supporting Information shows the  $\text{N}_2$  adsorption–desorption isotherm of 3-D  $\text{SnO}_2$ –RGO architecture. Similarly with  $\text{SnO}_2$ /RGO composite, there exists a knee for the first adsorption step around the relative vapor pressure of 0.1. However, 3-D  $\text{SnO}_2$ –RGO architecture shows no hysteresis loop; this is clear evidence of reversible capillary condensation.<sup>19</sup> The formation of mesopore is also certified from pore size distribution shown in inset of Figure S3b in the Supporting Information. Unlike the  $\text{SnO}_2$ /RGO composite, 3-D  $\text{SnO}_2$ –RGO architecture does exhibit the broad pore size distribution and the higher BET surface area of  $315 \text{ m}^2 \text{ g}^{-1}$  while displaying a similar pore volume of  $0.15 \text{ cm}^3 \text{ g}^{-1}$ .

Similarly, we could also synthesize 3-D MO–RGO structures using the same procedure; however, metallic salts containing vanadium(II) and ruthenium(III) ions were used in this case

(Figure S4 in the Supporting Information). The  $\text{SnO}_2$  loading in the composite samples was determined using thermogravimetric analysis (TGA) (Figure S5a in the Supporting Information). Representative XRD patterns for GO and the 3-D  $\text{SnO}_2$ –RGO composite and the standard XRD pattern corresponding to  $\text{SnO}_2$  (JCPDS card no. 72-1147)<sup>20,21</sup> are shown in Figure S5b in the Supporting Information. For the GO powder, the broad diffraction peak at  $10.3^\circ$  is a typical peak for a GO specimen, corresponding to a *d*-spacing of about 0.83 nm.<sup>22</sup> This measured distance could be attributed to an approximately one-molecule-thick layer of water that is presumably hydrogen-bonded between the GO sheets. In contrast, the 3-D structure of the  $\text{SnO}_2$ –RGO architecture does not exhibit a GO peak but instead a broadened peak at  $24^\circ$  corresponding to the (002) plane of graphite, indicating the successful reduction of GO to RGO.<sup>23–25</sup> All the TEM images clearly show that the  $\text{SnO}_2$  nanoparticles are uniformly dispersed on the surface of the RGO sheets (Figure S5c in the Supporting Information).

The 3-D structure of the 65 wt %  $\text{SnO}_2$ –RGO composite exhibits a well-defined interconnected microstructure with uniformly dispersed micropores of several micrometers in size, as evidenced by the SEM images in Figure 3a,b (see also Figure S6 in the Supporting Information). Interestingly, many of these nanoparticles are homogeneously anchored on the RGO sheets, as indicated by energy-dispersive X-ray (EDX) elemental analysis (Figure S7 in the Supporting Information). Furthermore, the surface and TEM cross-sectional views in Figure 3c (and Figure S8 in the Supporting Information) reveal that the 3-D structure of the  $\text{SnO}_2$ –RGO composite contains not only micropores but also nanopores.

The TEM images in Figure 3d,e show that all of the 2–3 nm nanoparticles are anchored on the thin RGO sheets. In particular, the 3-D structure did not show any evidence of disassociated particles, and  $\text{SnO}_2$  nanoparticles covered the

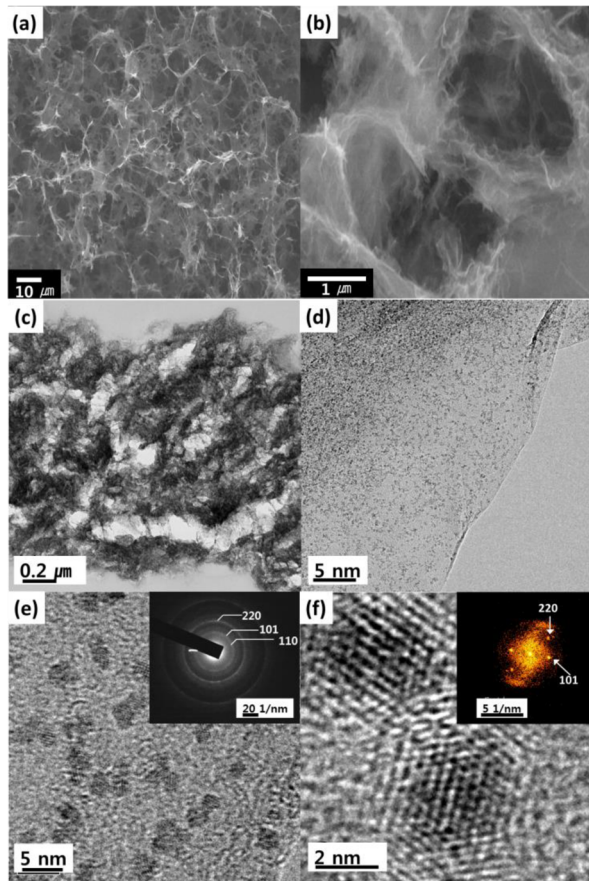


**Figure 3.** (a and b) SEM images of 65 wt % 3-D networked  $\text{SnO}_2$ –RGO composites, taken at 500 $\times$  and 10000 $\times$  magnification, respectively. (c) TEM cross-sectional image. (d and e) TEM plan-view image. The inset shows the corresponding SAED ring pattern. The four distinct diffraction rings correspond to the (110), (101), (200), and (210) crystalline planes of  $\text{SnO}_2$ , indicating highly crystalline  $\text{SnO}_2$  nanoparticles. (f) High-resolution TEM images of the same materials taken at 500000 $\times$  and 1500000 $\times$  magnification, respectively. The inset shows the corresponding FFT pattern.

entire surface of the RGO sheets. The selected-area electron diffraction (SAED) pattern in the inset of Figure 3e has four distinct diffraction rings corresponding to the (110), (101), (200), and (210) crystalline planes of  $\text{SnO}_2$ , indicating that the  $\text{SnO}_2$  nanoparticles are highly crystalline.<sup>26,27</sup> Further investigation using high-resolution transmission electron microscopy (HRTEM) further confirmed the highly crystalline nature of the  $\text{SnO}_2$  nanoparticles in the composites, as shown in Figure 2f.<sup>26</sup> From the XRD patterns, the mean crystallite size of  $\text{SnO}_2$  estimated using the Scherrer equation<sup>28</sup> was found to be approximately 2.21 nm on the basis of the (110) peak (Table 1 in Supporting Information); this value is consistent with the TEM characterization results. Moreover, the fast Fourier transform (FFT) electron diffraction pattern for the particles shown in the inset further demonstrates their high degree of crystallinity.

The as-synthesized and reduced GO was analyzed by XPS in order to observe the evolution of the oxygen functional groups. From the C 1s XPS spectra, it is clear that the proportion of carbon–carbon (C–C) bonds increases when the GO is reduced in the  $\text{SnO}_2$ –RGO composite.<sup>23,24</sup> More specifically, the intensity of the C–OH peak dramatically decreases when the GO is reduced by the tin salt (Figure S19 in the Supporting

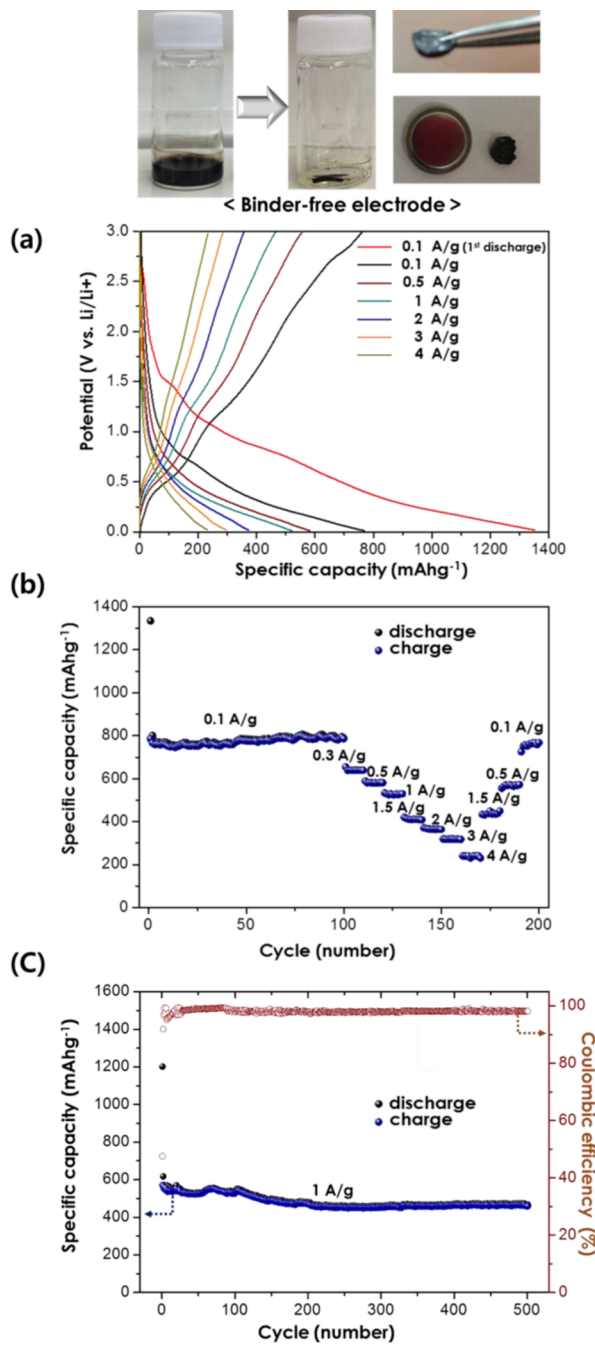
Information). As shown in the inset of Figure S10 in the Supporting Information, the Sn 3d<sub>5/2</sub> and Sn 3d<sub>3/2</sub> peaks associated with the  $\text{SnO}_2$  nanoparticles are located at 487.5 and 495.9 eV, further suggesting the formation of  $\text{SnO}_2$  nanoparticles coupled with the RGO sheets. Moreover, the amount of C–OH and C–O–C groups in the composite was significantly lower than what was expected based on the intensity of the peak located at 533.4 eV in the O 1s spectrum for the pristine GO (Figure S11 in the Supporting Information). This suggests that the hydrogen in the hydroxyl groups or possibly the Sn 3d<sub>5/2</sub> electrons in  $\text{SnO}_2$  were replaced to form an O–Sn<sup>4+</sup> connection and open the epoxy group rings.<sup>26</sup> Thus, the extra peak at 530.2 eV was attributed to the formation of an O–Sn<sup>4+</sup> bond. It is also possible that the Sn 3d<sub>5/2</sub> electrons may bind with RGO at oxygen-containing functional groups on the RGO surface. FT-IR was used to determine any changes in the functional groups of the GO surface during the tin salt reduction process.

Figure S12 in the Supporting Information shows that the absorption band corresponding to C–O stretching is markedly less intense for the RGO. Furthermore, the C–C peak (1625  $\text{cm}^{-1}$ ) is shifted to 1610  $\text{cm}^{-1}$ , most likely by a restoration of the  $sp^2$  structure in the 3-D architecture<sup>23,27</sup> and some of the adsorbed water molecules.<sup>28</sup> These results suggest that  $\text{SnO}_2$  nanoparticles grown on these functional groups are anchored to the GO and partially reduce it, thereby recovering some of the original C=C bonds.<sup>18</sup> Coupled with the XPS findings, that the RGO exhibits a “self-healing” behavior, as explained below.

Figure S13 in the Supporting Information compares the Raman spectra of GO and 3-D  $\text{SnO}_2$ –RGO composites prepared with different ratios of  $\text{SnCl}_2$  and GO. For both materials, disordered (D) and graphitic (G) carbonaceous Raman bands are observed at 1350 and 1580  $\text{cm}^{-1}$ , respectively.<sup>24,25,29</sup> The spectra of the 3-D  $\text{SnO}_2$ –RGO architecture exhibit a higher D/G intensity ratio than GO. It may be due to a decrease in the average size of the  $sp^2$  domains upon the reduction of the exfoliated GO and is probably because new graphitic domains are created that are smaller in size than the ones present in GO before reduction, but greater in number. The bands observed at  $\sim$ 630, 688, and 770  $\text{cm}^{-1}$  are related to the  $A_{1g}$ ,  $A_{2u}$ , and  $B_{2g}$  vibration modes of  $\text{SnO}_2$ , respectively.<sup>24,25</sup> During the reduction of GO, the G peak was blue-shifted for the RGO.<sup>22,26,27</sup> A notable fact was that while the G band peak was located at a higher frequency in GO than in graphite, but after reducing RGO or graphene, it was located at almost the same frequency as that in graphite. Therefore, in RGO, the G band shifted back to the position of the G band in graphite. Therefore, in RGO, the G band is clearly shifted back by a graphitic “self-healing” that is similar to that observed by the sharpening of the G peak and the intensity increase of the D peak in reduced graphene oxide.

Because of the high conductivity, large surface area, and porous texture of graphene, it has been increasingly used in Li-ion batteries (LIBs) as a flexible confinement structure to provide a buffering capability to reduce electrode pulverization. The use of  $\text{SnO}_2$  and its composites as anode materials has also attracted considerable attention because of their high  $\text{Li}^+$  storage capacities.<sup>17</sup> Hence, the electrochemical properties of a 65 wt %  $\text{SnO}_2$ –RGO 3-D architecture were investigated to evaluate its effectiveness as an electrode material.

Figure 4 shows the results obtained for a coin-type half-cell Li-ion battery with a 3-D  $\text{SnO}_2$ –RGO architecture as a binder-free electrode. The charge–discharge curves of this cell in



**Figure 4.** (a) Charge–discharge curves for a binder-free, 65 wt % 3-D  $\text{SnO}_2$ –RGO half-cell showing its rate capability at different current rates (from right to left: 0.1, 0.5, 1, 2, 3, and 4  $\text{A g}^{-1}$ ). (b) Rate capability at different current rates (from left to right: 0.1, 0.3, 0.5, 1, 1.5, 2, 3, and 4  $\text{A g}^{-1}$ ). (c) Cyclability of a 3-D  $\text{SnO}_2$ –RGO nanostructure measured at 1  $\text{A g}^{-1}$  over 500 cycles.

Figure 4a,b clearly demonstrates its good charge/discharge capacity retention and rate performance. In the initial cycle at 0.1  $\text{A g}^{-1}$ , a strong cathodic peak is observed at 0.75 V that can be ascribed to the formation of solid electrolyte interphase layers on the surface of the active material, the reduction of  $\text{SnO}_2$  to Sn, and the synchronous formation of  $\text{Li}_2\text{O}$ . The peak near 0 V results from Li intercalation into graphene to form  $\text{LiC}_6$ , whereas the other relatively weak peaks located between 0.75 and 0 V can be ascribed to the formation of  $\text{Li}_x\text{Sn}_y$  compounds (e.g.,  $\text{Li}_2\text{Sn}_5$ ,  $\text{LiSn}$ ,  $\text{Li}_7\text{Sn}_3$ ,  $\text{Li}_5\text{Sn}_2$ , and  $\text{Li}_{22}\text{Sn}_5$ ).<sup>21</sup>

In the anodic curve, the peaks at 0.2, 0.5, and 1.26 V are attributed to Li deintercalation from  $\text{LiC}_6$ , Li dealloying from  $\text{Li}_x\text{Sn}$ , and the partially reversible reaction from Sn to  $\text{SnO}_2$ , respectively. The high capacity of ~240  $\text{mAh g}^{-1}$  even at a current density of 4  $\text{A g}^{-1}$  is made possible by the highly conductive RGO sheets in the hybrid electrode, which serve as electrically conductive channels for the  $\text{SnO}_2$  nanoparticles. As shown as Figure 4b, after this rigorous test process, the electrode can recover to its initial value of 770  $\text{mAh g}^{-1}$  when the current density returns to 0.1  $\text{A g}^{-1}$ , exhibiting good capacity retention ability. Supporting Information Figure S14 shows cyclic voltammograms (CVs) for the devices scanned at 0.1, 0.5, and 1  $\text{mV s}^{-1}$  in the range 0–3 V. Interestingly, the general shape of these CVs<sup>17</sup> is maintained despite the increase in the potential scan rate, further indicating that the 3-D  $\text{SnO}_2$ –RGO architecture electrode possesses good high-rate capabilities. The cycle performance of the 3-D  $\text{SnO}_2$ –RGO architecture was further investigated at a current density of 1  $\text{A g}^{-1}$ , as shown in Figure 4 c. From these results, we can see that the 3-D  $\text{SnO}_2$ –RGO structure exhibits good cycle stability and capacity retention of 86% at 1  $\text{A g}^{-1}$  after 500 cycles. In addition, the Coulombic efficiency remained at approximately 98%, except during the first cycle. The improved performance of the 3-D  $\text{SnO}_2$ –RGO should be attributed to the following factors: (i) 3-D architecture that provides the advantages of continuous porosity, high surface area that gives an increase to a large contact area between the active material and the electrolyte and the architecture that provides fast transport pathways for the electrolyte ions; (ii) RGO nanosheets that provide a highly conductive matrix for electron transfer during the lithiation and delithiation processes; and (iii) the intimate interaction between  $\text{SnO}_2$  nanoparticles and RGO nanosheets, which combined with the uniform mixture prevents both the aggregation of  $\text{SnO}_2$  nanoparticles and the restacking of the RGO nanosheets.<sup>30</sup>

## CONCLUSIONS

In this study, we have demonstrated the effectiveness of controlling the graphene oxide (GO) reduction conditions for simple *in situ* synthesis of a three-dimensional (3-D) metal oxide (MO)–reduced graphene oxide (RGO) architecture. Furthermore, it has been shown that a tin salt can function not only as a reducing agent to convert conventional RGO to a highly conductive 3-D RGO structure but also as a precursor for  $\text{SnO}_2$  nanoparticles. In this way, a 3-D  $\text{SnO}_2$ –RGO composite was successfully achieved in which  $\text{SnO}_2$  particles measuring a few nanometers (2–3 nm) in size were confirmed to be adsorbed between the RGO nanosheets. The  $\text{SnO}_2$  was successfully synthesized by controlling the conditions to make the two reactions (RGO reduction and synthesis of  $\text{SnO}_2$ ) occur simultaneously. Moreover, when applied as a binder-free  $\text{SnO}_2$ –RGO electrode, this newly synthesized material demonstrated a high reversible capacity of 796  $\text{mAh g}^{-1}$  at 0.1  $\text{A g}^{-1}$  (over 100 deep charge–discharge cycles) and a high-rate capacity of 250  $\text{mAh g}^{-1}$  at 4  $\text{A g}^{-1}$ .

In addition, this study demonstrated 3-D structures based on  $\text{SnO}_2$ –RGO,  $\text{V}_2\text{O}_5$ –RGO, and  $\text{RuO}_2$ –RGO composite systems, so it is believed that this approach to reduction synthesis by means of a metal salt could be readily applied to other metal oxide–RGO hybrid nanostructures in order to study their synergistic properties.

**■ ASSOCIATED CONTENT****S Supporting Information**

Figures S1–S14 and Table S1 showing supporting results from additional experiments. This material is available free of charge via the Internet at <http://pubs.acs.org>.

**■ AUTHOR INFORMATION****Corresponding Authors**

\*(R.C.R.) E-mail: rkc@kicet.re.kr.

\*(K.-B.K.) E-mail: kbkим@yonsei.ac.kr.

**Author Contributions**

The manuscript was written through contributions of all authors. All authors have given approval to the final version of the manuscript.

**Notes**

The authors declare no competing financial interest.

**■ ACKNOWLEDGMENTS**

This work was supported by the energy efficiency and resources grant (No: 20122010100140 and No: 20122010100090) of the Korea Institute of Energy Technology Evaluation and Planning (KETEP) funded by the Ministry of Knowledge Economy, Korean government.

**■ REFERENCES**

- (1) Geim, A. K.; Novoselov, K. S. *Nat. Mater.* **2007**, *6*, 183.
- (2) Zhu, Z. P.; Su, D. S.; Weinberg, G.; Schlogl, R. *Nano Lett.* **2004**, *4*, 2255.
- (3) Wang, H. L.; Wang, X. R.; Li, X. L.; Dai, H. J. *Nano Res.* **2009**, *2*, 336.
- (4) Liu, F.; Seo, T. S. *Adv. Funct. Mater.* **2010**, *20*, 1930.
- (5) Chen, Z.; Ren, W.; Gao, L.; Liu, B.; Pei, S.; Cheng, H. M. *Nat. Mater.* **2011**, *10*, 424.
- (6) Xu, Y.; Wu, Q.; Sun, Y.; Bai, H.; Shi, G. *ACS Nano* **2010**, *4*, 7358.
- (7) Tang, Z.; Shen, S.; Zhuang, J.; Wang, X. *Angew. Chem., Int. Ed.* **2010**, *19*, 6306.
- (8) Jiang, X.; Ma, Y. W.; Li, J. J.; Fan, Q. L.; Huang, W. *J. Phys. Chem. C* **2010**, *114*, 22462.
- (9) Bai, H.; Li, C.; Shi, G. *Q. Adv. Mater.* **2011**, *23*, 1089.
- (10) Das, B.; Choudhury, B.; Gomathi, A.; Manna, A.; Pati, S.; Rao, C. *ChemPhysChem* **2011**, *12*, 937.
- (11) Scheuermann, G. M.; Rumi, L.; Steurer, P.; Bannwarth, W.; Mulhaupt, R. *J. Am. Chem. Soc.* **2009**, *131*, 8262.
- (12) Vedala, H.; Sorescu, D. C.; Kotchey, G. P.; Star, A. *Nano Lett.* **2011**, *11*, 2342.
- (13) Wang, X.; Tang, Z. H.; Shen, S. L.; Zhuang, J. *Angew. Chem., Int. Ed.* **2010**, *49*, 4603.
- (14) Chen, X.; Li, S.; Chen, C.; Yan, L. *Adv. Mater.* **2011**, *23*, 5679.
- (15) Cong, H. P.; Ren, X. C.; Wang, P.; Yu, S. H. *ACS Nano* **2012**, *2693*.
- (16) Park, S. H.; Kim, H. K.; Ahn, D. J.; Lee, S. I.; Roh, K. C.; Kim, K. B. *Electrochem. Commun.* **2013**, *34*, 117.
- (17) Wen, Z.; Wang, Q.; Zhang, Q.; Li, J. *Adv. Funct. Mater.* **2007**, *17*, 2772.
- (18) Stankovich, S.; Dikin, D. A.; Piner, R. D.; Kohlhaas, K. A.; Kleinhammes, A.; Jia, Y.; Wu, Y.; Nguyen, S. T.; Ruoff, R. S. *Carbon* **2007**, *45*, 1558.
- (19) Mikhail, R. S.; Brunauer, S.; Bodor, E. E. *J. Colloid Interface Sci.* **1968**, *26*, 54.
- (20) Kim, H. K.; Bak, S. M.; Kim, K. B. *Electrochem. Commun.* **2010**, *12*, 1768.
- (21) Zhang, M.; Lei, D.; Du, Z.; Yin, X.; Chen, L.; Li, Q.; Wang, Y.; Wang, T. *J. Mater. Chem.* **2011**, *21*, 1673.
- (22) Zhu, Y.; Murali, S.; Cai, W.; Li, X.; Suk, J. W.; Potts, J. R.; Ruoff, R. S. *Adv. Mater.* **2010**, *22*, 3906.
- (23) Stankovich, S.; Piner, R. D.; Chen, X.; Wu, N.; Nguyen, S. T.; Ruoff, R. S. *J. Mater. Chem.* **2006**, *16*, 155.
- (24) Dreyer, D. R.; Park, S. J.; Bielawski, C. W.; Ruoff, R. S. *Chem. Soc. Rev.* **2010**, *39*, 228.
- (25) Stankovich, S.; Dikin, D. A.; Piner, R. D.; Kohlhaas, K. A.; Kleinhammes, A.; Jia, Y.; Wu, Y.; Nguyen, S. T.; Ruoff, R. S. *Carbon* **2007**, *45*, 1558.
- (26) Wen, Z.; Cui, S.; Kim, H.; Mao, S.; Yu, K.; Lu, G.; Pu, H.; Mao, O.; Chen, J. *J. Mater. Chem.* **2012**, *22*, 3300.
- (27) Li, Y.; Lv, X.; Lu, J.; Li, J. *J. Phys. Chem. C* **2010**, *114*, 21770.
- (28) Yang, D.; Zhou, L.; Chen, L.; Zhao, B.; Zhang, J.; Li, C. *Chem. Commun.* **2012**, *48*, 8078.
- (29) Kudin, K. N.; Ozbas, B.; Schniepp, H. C.; Prud'homme, R. K.; Aksay, I. A.; Car, R. *Nano Lett.* **2008**, *8*, 36.
- (30) Huang, Y.; Wu, D.; Han, S.; Li, S.; Xiao, L.; Zhang, F.; Feng, X. *ChemSusChem* **2013**, *6*, 1510.